Clim Dyn (2018) 51:1585–1603
DOI 10.1007/s00382-017-3972-7

On the sensitivity of Antarctic sea ice model biases to atmospheric forcing uncertainties

Antoine Barthélemy[1] · **Hugues Goosse**[1] · **Thierry Fichefet**[1] · **Olivier Lecomte**[1]

Received: 27 March 2017 / Accepted: 10 October 2017 / Published online: 3 November 2017

Abstract Although atmospheric reanalyses are an extremely valuable tool to study the climate of polar regions, they suffer from large uncertainties in these data-poor areas. In this work, we examine how Antarctic sea ice biases in an ocean-sea ice model are related to these forcing uncertainties. Three experiments are conducted in which the NEMO-LIM model is driven by different atmospheric forcing sets. The minimum ice extent, the ice motion and the ice thickness are sensitive to the reanalysis chosen to drive the model, while the wintertime ice extent and inner pack concentrations are barely affected. The analysis of sea ice concentration budgets allows identifying the processes leading to differences between the experiments, and also indicates that large and similar errors compared to observations are present in all three cases. Our assessment of the influence of forcing inaccuracies on the simulated Antarctic sea ice allows disentangling two types of model biases: the ones that can be reduced thanks to better atmospheric forcings, and those that would require improvements of the physics of the ice or ocean model.

Keywords Sea ice · Antarctic · Model · Atmospheric forcing · Uncertainties

✉ Antoine Barthélemy
antoine.barthelemy@uclouvain.be

[1] Georges Lemaître Centre for Earth and Climate Research (TECLIM), Earth and Life Institute (ELI), Université catholique de Louvain (UCL), Louvain-la-Neuve, Belgium

1 Introduction

To date, accurately representing the Antarctic sea ice in climate models is still a scientific challenge. CMIP5 coupled models fail to capture the slight increase in ice extent observed over the last decades (Turner et al. 2013), and they do not simulate properly the mean state and variability of the ice cover (Zunz et al. 2013; Shu et al. 2015). Ocean-sea ice models forced by atmospheric reanalyses also present large biases, for instance in ice motion (Massonnet et al. 2011; Uotila et al. 2014; Lecomte et al. 2016). Yet, the sea ice plays a central role in the dynamics of the Southern Ocean, which is itself a key player in the global climate system, being a sink for anthropogenic carbon and uptaking a large part of the heat trapped because of the increase in greenhouse gas concentrations in the atmosphere. Improvements are therefore required in models not only to better understand the ongoing changes in Antarctic sea ice (Hobbs et al. 2016), but also to produce more reliable climate projections (e.g., Bracegirdle et al. 2015).

However, identifying the reasons behind the improper representation of Antarctic sea ice in current models is not straightforward. Earlier studies have highlighted that the quality of simulations in the Southern Ocean is less impacted by sea ice model physics (Massonnet et al. 2011; Uotila et al. 2017) or parameters (Uotila et al. 2012) than in the Arctic. Indeed, the mostly seasonal and divergent nature of the Antarctic ice pack makes it more dependent on the atmospheric and oceanic forcings. Improving our understanding of the influence of these forcings on the simulated sea ice should ultimately help to pave the way towards more skillful models.

In polar regions, an invaluable source of information about the state of the atmosphere is supplied by reanalyses. Using data assimilation to constrain atmospheric models,

they provide the long-term and spatially-complete forcing fields that are needed to drive ocean-sea ice models. These can then be used to study sea ice processes in a simpler modeling context than with fully coupled systems. Nevertheless, the sparsity of data at high latitudes implies large uncertainties in the reanalyses, especially in the Antarctic (e.g., Bromwich et al. 2007; Wang et al. 2016). Over the seasonally ice-covered Southern Ocean, the lack of observations available for assimilation is even more pronounced. This results in significant biases in the reanalyses, although the evaluation of the latter against independent datasets is difficult and often restricted to limited areas and periods (Vihma et al. 2002; Vancoppenolle et al. 2011; Jones et al. 2016).

The sensitivity of ocean-sea ice models to atmospheric forcing inaccuracies has been addressed in previous studies. Hunke and Holland (2007) have shown that, when forced by datasets sharing many similarities, simulations of the Arctic sea ice nevertheless presented clear differences, most notably in ice thickness and ocean circulation. Lindsay et al. (2014) have also demonstrated that forcing an Arctic ocean-sea ice model with different atmospheric reanalyses led to varying agreements with existing ice thickness observations and to changes in the modeled long-term trend in total ice volume. Chaudhuri et al. (2016) have quantified the differences in ocean model simulations due to atmospheric uncertainties, and they have shown that these differences were substantial for cryospheric surface variables mainly in the marginal ice zones.

In this work, our objective is to assess specifically the sensitivity of Antarctic sea ice simulations to uncertainties in the atmospheric forcing. We do not aim directly at evaluating the reanalyses against independent observations, but rather to determine to which extent sea ice biases in the mean state of forced models can be attributed to inaccurate forcing fields. The results allow to identify the aspects of Southern Ocean sea ice simulations that can be improved thanks to better drivers, and those that require efforts in other directions, such as developments of the sea ice model physics or enhancements of the ocean model performance. To fulfill this goal, the global ocean-sea ice model NEMO-LIM is driven by three atmospheric reanalyses, the differences between the simulations are thoroughly analyzed and the results are compared to observational datasets. We go beyond the simple comparison between model variables and observations by making use of ice concentration budgets, which allow us to gain insights into the processes driving the seasonal evolution of the sea ice cover in each simulation.

This paper is organized as follows. The model setup is presented in Sect. 2, including descriptions of NEMO-LIM and of the three atmospheric reanalyses used. Observational data utilized to evaluate model outputs are documented in Sect. 3. Our results are then described and discussed in Sect. 4, while a summary of our findings and concluding remarks are finally given in Sect. 5.

2 Model setup

2.1 Ocean-sea ice model NEMO-LIM

The present study is conducted using version 3.6 of the state-of-the-art ocean modeling framework NEMO (Nucleus for European Modelling of the Ocean, Madec 2008). It includes a finite-difference, hydrostatic, free-surface, primitive-equation ocean model, which is coupled to the dynamic-thermodynamic sea ice model LIM3.6 (Louvain-la-Neuve sea Ice Model, Rousset et al. 2015) to form the NEMO-LIM system.

LIM incorporates an ice thickness distribution (ITD), which represents the subgrid-scale heterogeneity of ice thickness, enthalpy and salinity, and an advanced halodynamics scheme, which makes the sea ice salinity variable in space and in time (Vancoppenolle et al. 2009). The ice dynamics are computed based on an elastic–viscous–plastic rheology formulated on a C-grid (Bouillon et al. 2013). The ice-ocean coupling is extensively described in Barthélemy et al. (2016a). Turbulent vertical mixing in the ocean is handled with the so-called TKE scheme (Blanke and Delecluse 1993). Static instabilities are removed thanks to an enhanced vertical diffusion scheme. The parameterization of mesoscale eddies follows Gent and Mcwilliams (1990).

2.2 Atmospheric forcing sets

This study makes use of three different atmospheric reanalysis products. The first two reanalyses (DFS5.2 and JRA-55, see below) are utilized within the CORE forcing formulation of NEMO-LIM, in which the ocean surface boundary conditions are computed on the basis of bulk formulae developed by Large and Yeager (2004). The required atmospheric fields are the air temperature, the specific humidity, the zonal and meridional components of the wind, the incoming longwave and shortwave radiations, and the total and solid precipitation rates.

The DRAKKAR Forcing Set version 5.2 (DFS5.2, Dussin et al. 2016) is based on the ERA-Interim reanalysis over 1979–2015. An extension based on ERA-40 exists for the period 1958–1978. The spatial resolution is close to 0.7°, or 80 km. A number of corrections to the original fields are implemented in order to improve their agreement with observational datasets (Brodeau et al. 2010). For instance, a warm bias of ERA-Interim at high southern latitudes is reduced through a cooling increasing by 0.13 °C per degree of latitude between 60 and 75°S, which yields a correction of 2 °C at 75°S. Air temperature, humidity and

wind are provided at a 3-hourly frequency, while radiation and precipitation have a daily frequency.

The Japanese 55-year Reanalysis (JRA-55, Kobayashi et al. 2015) is produced with the Japan Meteorological Agency operational system as of December 2009. It covers the period 1958–2015. A sophisticated four-dimensional variational data assimilation method and a high spatial resolution are used. The TL319L60 model grid corresponds to a horizontal resolution of approximately 60 km. All forcing fields are available at a 3-hourly frequency.

A second forcing formulation, called CLIO, is based on simpler bulk formulae introduced by Goosse (1997). The air temperature, the specific humidity, the zonal and meridional components of the wind stress, the wind speed, the cloud cover and the total precipitation are needed as input fields. The radiative fluxes are derived from the cloud cover. In the present work, we use the National Centers for Environmental Prediction/National Center for Atmospheric Research Reanalysis 1 (NCEP/NCAR, Kalnay et al. 1996) with this CLIO formulation. This reanalysis is produced with a frozen global data assimilation system from January 1995. It covers the period 1948 to the present and is updated daily. Its horizontal resolution is T62, which is around 210 km. In our simulations forced with NCEP/NCAR, the fields that we use from the reanalysis are air temperature and winds, at a daily frequency. The wind speeds are converted into wind stresses using a quadratic bulk formula with a constant drag coefficient of 1×10^{-3}. Since humidity, cloudiness and precipitation are of questionable reliability in the NCEP/NCAR reanalysis, these fields are extracted from monthly climatologies (Trenberth et al. 1989; Berliand and Strokina 1980; Large and Yeager 2004, respectively) and interpolated in time between the monthly values. This formulation and the selected climatological fields are identical to the ones used in many past simulations with NEMO-LIM, allowing a comparison with previous studies (e.g., Vancoppenolle et al. 2009; Massonnet et al. 2011; Barthélemy et al. 2016a; Lecomte et al. 2016).

In the following, the three atmospheric forcing sets are simply referred to as DFS, JRA and NCEP. Table 1 summarizes their characteristics.

2.3 Experimental design

Three NEMO-LIM global ocean-sea ice experiments are conducted, which differ only by their atmospheric forcing. Their names correspond to those of the forcing sets. For consistency, all simulations start in January 1958, when the data from DFS and JRA become available. They are initialized at rest with temperature and salinity fields from the World Ocean Atlas 2013 climatology (WOA13, Locarnini et al. 2013; Zweng et al. 2013). At initialization, regions where the sea surface temperature is within 2 °C of the freezing point are covered with ice with a concentration of 0.9, a thickness of 1 m and a salinity of 6.3 g/kg, and capped with a 0.3 m snow layer. The simulations are run until December 2015. Unless otherwise stated, their results are analyzed over the 30 year period from 1985 to 2014. A time span of 30 years is typical for climate studies, and we choose 2014 as the end year because the sea ice concentration observations that we use only exist until April 2015 (see Sect. 3). The relatively short spinup is sufficient for the sea ice and upper ocean to be close to equilibrium. It is likely not the case for the deep ocean, which will not be studied here.

The time step of the ocean model is equal to 1 h, but the surface boundary condition module, which includes the sea ice computations, is called every six time steps. The ITD in LIM is discretized into five thickness categories. North of 60°S, river runoff rates are derived from the climatological dataset of Dai and Trenberth (2002). Around Antarctica, the freshwater input of continental origin is made of two components. First, prescribed meltwater fluxes from ice shelves are discharged along the coastline into the ocean over spatially-varying depth ranges, following Depoorter et al. (2013). Second, the climatological freshwater flux from icebergs melt of Merino et al. (2016) is added at the surface of the Southern Ocean. In order to avoid spurious model drifts, a sea surface

Table 1 Characteristics of the three atmospheric forcing sets used in this study

Forcing set	DFS	JRA	NCEP
Atmospheric reanalysis	DFS5.2 (ERA-Interim/40)	JRA-55	NCEP/NCAR
NEMO-LIM forcing formulation	CORE	CORE	CLIO
Horizontal resolution	80 km	60 km	210 km
Period	1958–2015	1958–present	1948–present
Frequency of temp. and wind data	3 h	3 h	1 day
Frequency of humidity data	3 h	3 h	Climatological
Frequency of radiation and precip. data	1 day	3 h	Climatological
References	Dussin et al. (2016)	Kobayashi et al. (2015)	Kalnay et al. (1996)

The climatological fields indicated for NCEP are not derived from the NCEP/NCAR reanalysis itself (see text for details)

salinity restoring towards the WOA13 climatology (Zweng et al. 2013) is activated, with a time scale of 310 days for a 50 m mixed layer. It is however damped under sea ice proportionally to the concentration, in order to avoid altering the simulated ice–ocean interactions.

Both ocean and sea ice models are run on the eORCA1 grid, which is similar to the quasi-isotropic global tripolar grid ORCA1 traditionally used with NEMO (Madec and Imbard 1996). The slight changes aim at allowing the simulation of Antarctic under-ice shelf seas, which are not implemented in this study. The grid has a nominal resolution of 1° in the zonal direction. The vertical discretization in the ocean is based on a partial step z coordinate. The 75 layers increase non-uniformly in thickness from 1 m at the surface to 10 m at 100 m depth, and reach 200 m at the bottom. The ocean vertical resolution is significantly finer than in earlier studies with the same model (e.g., Barthélemy et al. 2016a). The effects of this modification are discussed in an "Appendix" to this paper.

3 Observational datasets

In this section, we describe the observations that are used to assess our model results and to put the differences between the experiments in perspective.

First, sea ice concentrations are obtained from version 1.2 of the EUMETSAT Ocean and Sea Ice Satellite Application Facility climate data record (OSISAF, EUMETSAT 2015). This reprocessed dataset covers the period October 1978 to April 2015. Ice concentrations are computed from atmospherically corrected passive microwave brightness temperatures from SMMR, SSM/I and SSMIS sensors, using a combination of state-of-the-art algorithms and dynamic tie-points (Tonboe et al. 2016), whose good performance has been acknowledged by Ivanova et al. (2015). The data are interpolated on the eORCA1 grid and monthly means are computed to facilitate the comparison with model outputs. In order to take observational uncertainties into account, the Antarctic sea ice extent values reported in the NSIDC Sea Ice Index (Fetterer et al. 2016) have also been retrieved. Covering the period 1978 to the present, they are derived from ice concentrations calculated thanks to the NASA Team algorithm (Cavalieri et al. 1996).

Uncertainties in sea ice drift observations are much larger than for concentration. Therefore, we also make use of two different products to evaluate the modeled ice speeds. The first is the Polar Pathfinder Daily 25 km EASE-Grid satellite dataset (Fowler et al. 2013) and the second is the one obtained from the Advanced Microwave Scanning Radiometer-Earth Observing System (AMSR-E, Kimura et al. 2013). As noted by Lecomte et al. (2016), the speeds in the second product are on average around 0.03 m s^{-1} larger than in the first, with the most pronounced differences occurring in the Weddell, Indian and Pacific free drift regions of the Southern Ocean. Evidence exists that the Fowler et al. (2013) data might be too slow (Heil et al. 2001).

4 Results and discussion

4.1 Sea ice concentration and extent

The mean seasonal cycles of Antarctic sea ice extent are shown in Fig. 1. While all experiments with different forcings overestimate the ice extent at the beginning of the

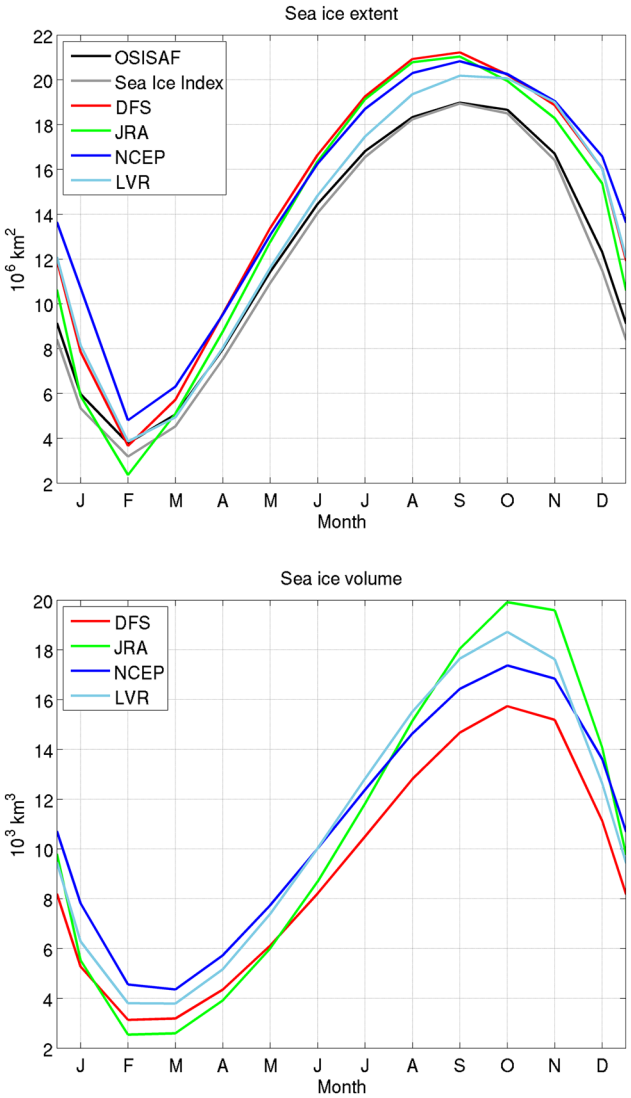

Fig. 1 Mean seasonal cycles of Antarctic sea ice extent (top) and volume (bottom), over 1985–2014, in the OSISAF (EUMETSAT 2015) and Sea Ice Index (Fetterer et al. 2016) observational products and in the different experiments. Experiment LVR is discussed in the "Appendix"

melting season, and while they remain close to each other until December, large differences appear in January and persist during summer. The two sets of observations that we use show an uncertainty of about 0.5×10^6 km^2 at the February minimum. DFS provides the closest match with both the OSISAF and Sea Ice Index extents, NCEP and JRA being approximately 1×10^6 km^2 above and below the DFS value, respectively.

In February, the Weddell Sea is the area where most of the remnant Antarctic sea ice lies. Thus, it is also where the simulated spatial distributions of ice concentration differ the most, between the model and the observations and between the simulations (Fig. 2). At the summer minimum in this region, ice is essentially confined in the western half of the Weddell Sea where it extends up to the northern tip of the Antarctic Peninsula. Ice does not extend as far north in the model, and experiments DFS and NCEP keep too much ice in the eastern Weddell Sea and along the coast of Dronning Maud Land. The three simulations share many similarities in the rest of the Southern Ocean. They lack the small patches of remnant ice along the coast of East Antarctica, perhaps as a result of the low resolution which prevents an accurate representation of the coastline. The opening of the Ross Sea polynya is reasonably well represented, with only a slight overestimation of the ice cover in this area. Finally, simulated ice concentrations are lower than observed in the Amundsen sea.

The differences in total sea ice extent between the experiments are particularly small during the ice expansion season (Fig. 1). All of them reach a maximum extent close to 21×10^6 km^2 in September, which is around 2×10^6 km^2 above the observed values. The distributions of sea ice concentration at the September maximum, displayed in Fig. 3, show that the overestimation of ice extent is widespread. The only region where the ice concentration in experiment DFS is lower than observed is around 140°

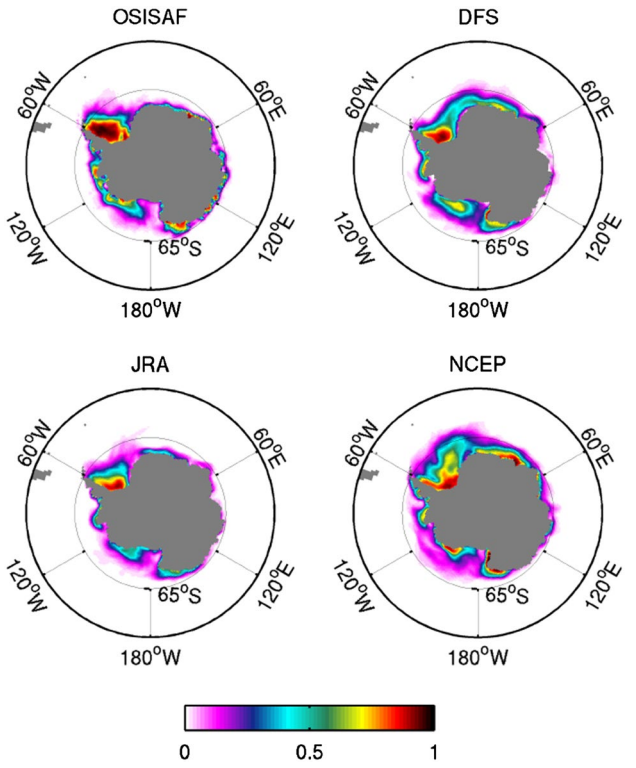

Fig. 2 February sea ice concentrations, averaged over 1985–2014, in the OSISAF observational product (EUMETSAT 2015) and in the different experiments

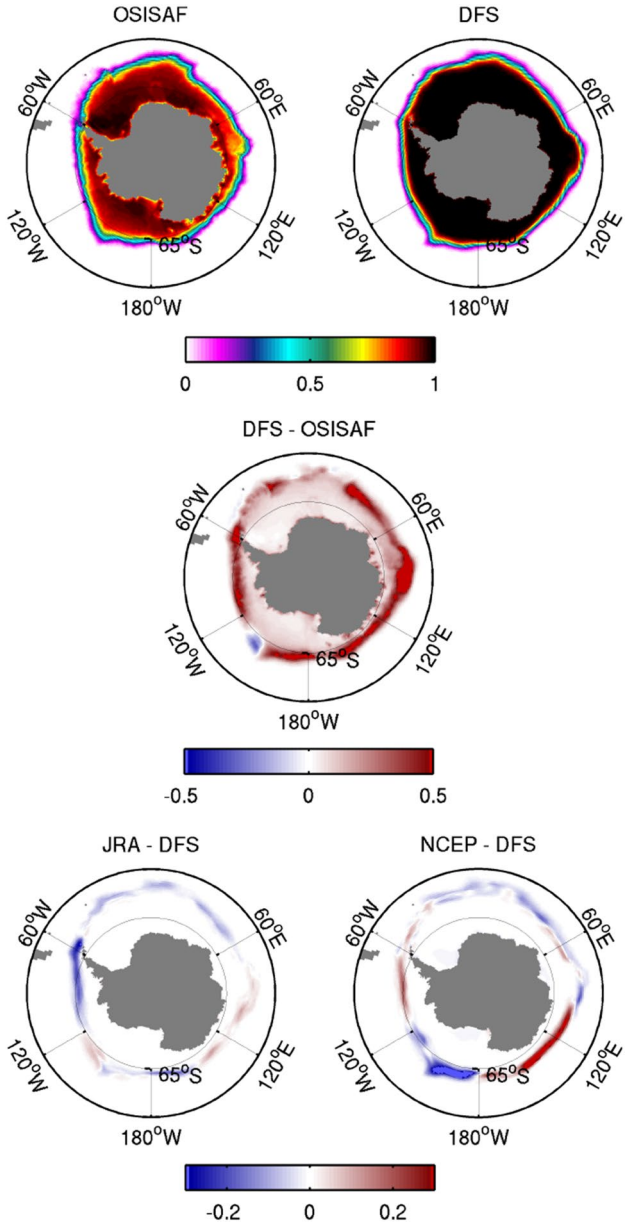

Fig. 3 September sea ice concentrations, averaged over 1985–2014, in the OSISAF observational product (EUMETSAT 2015), in experiment DFS and differences DFS-OSISAF, JRA-DFS and NCEP-DFS

W. Regardless of the forcing used to drive the model, the simulated sea ice concentrations are too high in coastal areas where polynyas exist in reality (e.g., Nihashi and Ohshima 2015). This discrepancy could be explained by an inadequate representation of coastal winds, in particular katabatic winds, in the low resolution atmospheric reanalyses used here (Stössel et al. 2011). Moreover, ice concentrations are overestimated by up to 10 % within the Antarctic sea ice pack. This issue was present in previous model versions as well (e.g., Vancoppenolle et al. 2009). It is sometimes mitigated by imposing an ad hoc maximum ice concentration, but this parameter has been kept at a high value of 99.9 % in this study.

As a result of the constantly high winter sea ice concentrations in the model, the differences induced by the forcing appear exclusively along the ice edge. Experiment JRA is similar to DFS, showing only weak changes in concentration, with the exception of a more pronounced decrease in the Bellingshausen Sea. NCEP differs more clearly from DFS. A dipole structure connects lower ice concentrations in the Ross and Amundsen Seas with higher ones in the Bellingshausen Sea. Between these two simulations, the other stark contrast is the larger sea ice extent from 90 to 180°E in NCEP.

Although our focus is mostly on the representation of the mean state of Antarctic sea ice, Table 2 gives some insight into the long-term trends and interannual variability of ice extent. The OSISAF (Sea Ice Index) dataset yields a positive trend in extent of 27×10^3 km^2 year^{-1} (28×10^3 km^2 year^{-1}). The simulated trends vary from 21×10^3 km^2 year^{-1} in NCEP to 48×10^3 km^2 year^{-1} in DFS, in spite of the fact that the atmospheric forcings are produced with the observed sea ice concentration fields as boundary condition. This demonstrates the importance of the forcing uncertainties in setting the long-term evolution of Antarctic sea ice. On the other hand, the model overestimates the summer variability for all forcings, while the magnitude of the winter variability is comparable to available observational estimates. Overall, the interannual variability is better represented than in CMIP5 coupled models (Zunz et al. 2013), which is expected for a forced model setup like ours.

4.2 Sea ice drift and wind stress

Recent studies have highlighted the role played by surface winds in the Antarctic sea ice dynamics, and have examined how this relates to the trends and biases in ice concentration (Holland and Kwok 2012; Uotila et al. 2014; Lecomte et al. 2016). Before looking at more advanced diagnostics, Fig. 4 shows the mean seasonal cycles of ice speed and of the norm of the wind stress, which is directly related to the wind speed by a quadratic bulk formula. The spatial averages for each month are computed in the area where the sea ice concentration is above 15 % in all simulations, to avoid displaying differences caused by an averaging over different regions in the three experiments. For the speed, the averaging is further restricted to the area where data are available in both observational products.

Both the sea ice speed and the wind stress peak in August and have their minimum close to the sea ice minimum in February. The link between the atmospheric dynamics and the ice speed is obvious all year long: with the strongest (weakest) winds, JRA (NCEP) presents the fastest (slowest) ice drift. The small gap between the DFS and JRA ice speeds between August and January can be explained by the higher ice thicknesses in the latter experiment during this period (see Figs. 1, 11), which tend to slow down the ice. Observational estimates of sea ice drift show large uncertainties, the Fowler et al. (2013) speeds being on average 0.03 m s^{-1} lower than the ones from Kimura et al. (2013). The best agreement with observations, especially those of Kimura et al. (2013), is obtained with experiment NCEP, which however slightly underestimates the amplitude of the seasonal cycle. While the latter is reasonably well represented in DFS and JRA, the ice speed in these experiments is between 0.03 and 0.06 m s^{-1} higher than in the Kimura et al. (2013) dataset.

4.3 Sea ice concentration budget

To gain a deeper understanding of the drivers of the seasonal development of Antarctic sea ice in the different simulations, we use online model diagnostics that split the total ice concentration changes at each time step into

Table 2 Antarctic sea ice trends and interannual variability over 1985–2014 in the OSISAF (EUMETSAT 2015) and Sea Ice Index (Fetterer et al. 2016) observational products and in the different experiments

Observations/experiment	OSISAF	Sea Ice Index	DFS	JRA	NCEP
Trend extent (10^3 km^2 year^{-1})	+ 27	+ 28	+ 48	+ 33	+ 21
Feb. extent variability (10^6 km^2)	0.44	0.41	0.70	0.66	0.91
Sep. extent variability (10^6 km^2)	0.51	0.36	0.31	0.29	0.40
Trend volume (km^3 year^{-1})	–	–	+ 36	+ 50	+ 40
Feb. volume variability (10^3 km^3)	–	–	0.60	0.84	0.84
Sep. volume variability (10^3 km^3)	–	–	0.69	0.87	0.63

The variability is computed as the standard deviation of the detrended anomalies

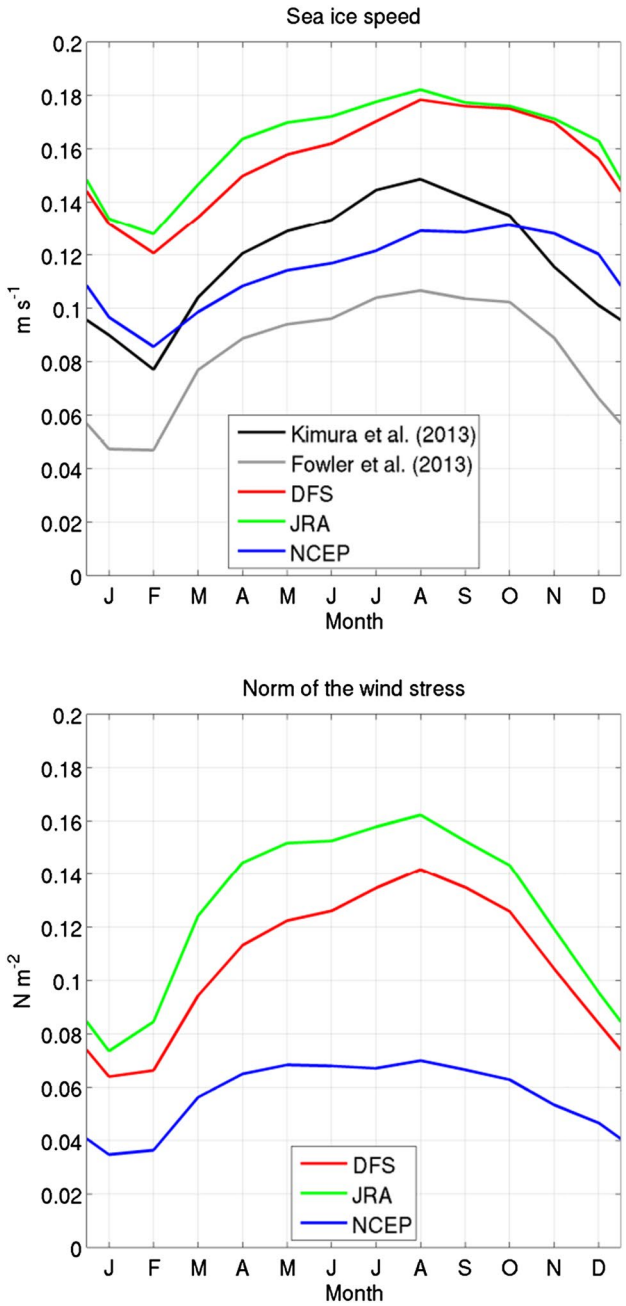

Fig. 4 Mean seasonal cycles of Antarctic sea ice speed in the Kimura et al. (2013) and Fowler et al. (2013) observational products and in the different experiments (top), and of the norm of the wind stress in the different experiments (bottom). The temporal mean is computed over 1985–2014 for the model simulations and over 2003–2010 for the observations, which corresponds to the period when the Kimura et al. (2013) product is available. Using the same period for the model experiments barely affects the diagnostics. For each month, the spatial average is computed in the area where the sea ice concentration is above 15 % in all simulations and, for the speed, where observations are available

dynamic and thermodynamic components. The general principle is close to the ice concentration budget developed by Holland and Kwok (2012), and applied to model results by Uotila et al. (2014) and Lecomte et al. (2016). The Holland and Kwok (2012) budget is designed for comparison with observations, which are not available during the ice melting season. While our online diagnostics cannot be evaluated against observational estimates, they can be analyzed in all seasons and have the further advantage to be computed during the simulation on the model grid, which allows a finer intercomparison between the experiments.

In our diagnostics of the sea ice concentration budget, the dynamic term includes the changes in concentration related to ice motion (advection and convergence/divergence) and mechanical redistribution (rafting and ridging). The foremost contributor to the thermodynamic term is the formation of new ice in open water. Bottom growth, bottom melt, surface melt and snow ice formation are vertical processes that have a direct impact on sea ice thickness. Since they also indirectly influence the total sea ice concentration, they contribute to the thermodynamic component of the budget as well. The ice concentration budget diagnostics are presented in Figs. 5 and 8, which show their spatial distributions, and in Table 3, which contains spatial averages in two selected domains. The first one corresponds to the ice pack interior, excluding ice edge areas. The second domain corresponds to coastal regions, defined as the grid cells located less than 25 km away from the coastline. Except for the northern tip of the Antarctic Peninsula, it is entirely included in the first domain.

The period chosen to examine the winter concentration changes runs from March to August, as these are the months during which the ice expands. The results presented in Fig. 5 and Table 3 for experiment DFS demonstrate two clear connections between dynamic and thermodynamic processes. First, within the sea ice pack, the thermodynamic expansion is tightly linked to the dynamics. In all regions but along the sea ice edge, the latter tend to lower the concentration through divergence, advection or mechanical deformation, which maintains open waters allowing heat losses to the atmosphere and seawater freezing. The dynamic trends are especially negative along the continent and are higher around West Antarctica. The dynamic decreases in sea ice concentration are balanced by thermodynamic growth, yielding a total change equal to 5.6×10^{-3} day^{-1} in regions where the concentration rises from 0 to a value close to 1 in 6 months. The second link is visible along the sea ice edge. There, advection tends to increase the ice concentration at lower latitudes, but this is mitigated by melt which occurs because ice is not thermodynamically sustainable in these warmer regions. These two connections are clearly visible in

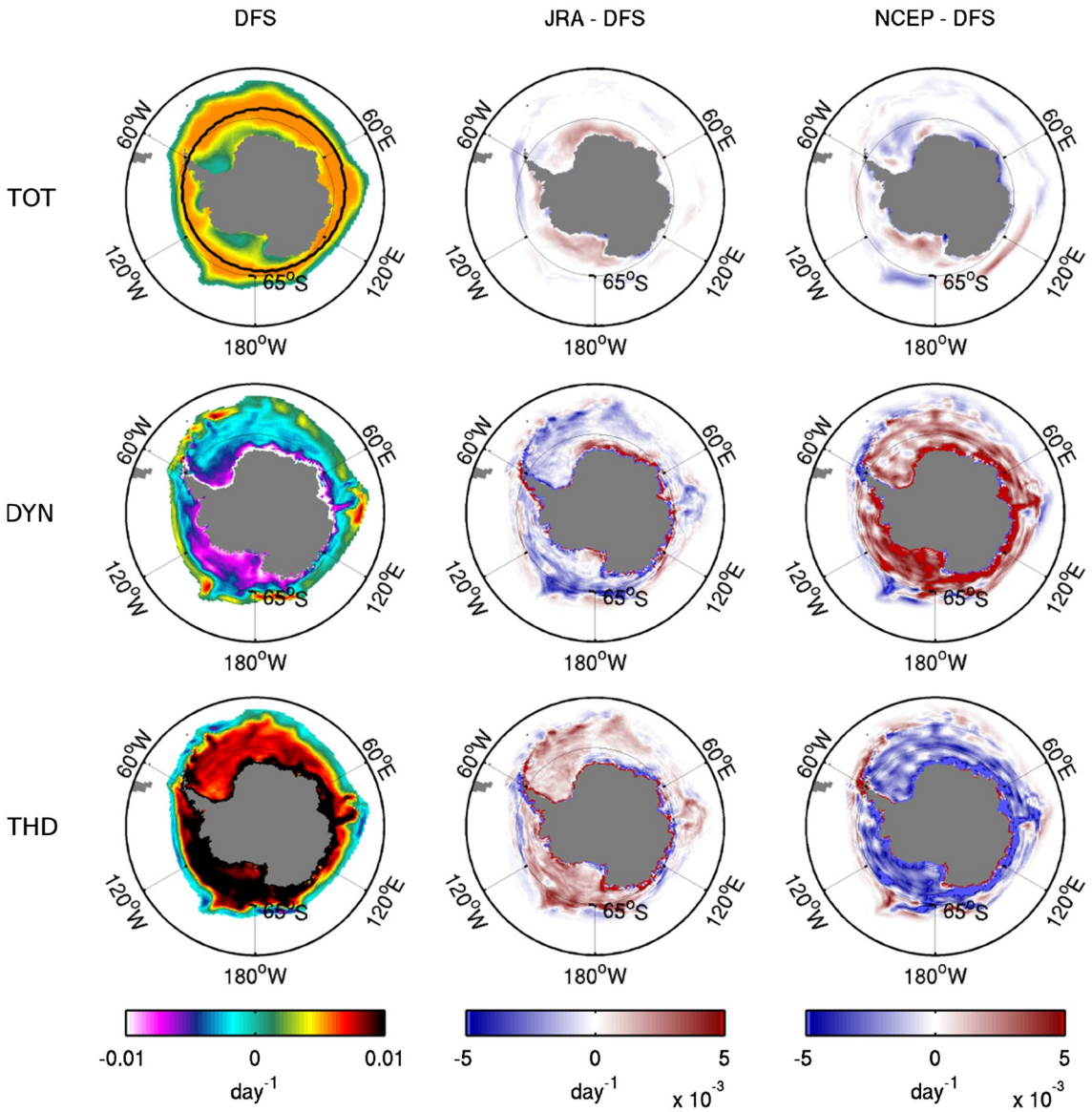

Fig. 5 Antarctic sea ice concentration budgets derived from online model diagnostics, averaged over March–August 1985–2014, in experiment DFS and differences JRA-DFS and NCEP-DFS. TOT, DYN and THD stand for the total concentration change, its dynamic part and its thermodynamic part, respectively. In the difference panels, red (blue) areas indicate stronger (weaker) ice concentration gains. The black line in the upper left panel delineates the interior domain over which spatial averages are computed in Table 3

the ice concentration budgets derived from observations as well (Holland and Kwok 2012; Holland and Kimura 2016).

Figure 5 also presents, for the diagnostics introduced above, the differences JRA-DFS and NCEP-DFS. These differences can be interpreted in light of Figs. 6 and 7, showing respectively the 2 m air temperature in the atmospheric reanalyses and the components of the wind stress over ice in the different experiments, averaged over the same time frame as the one used in Fig. 5. The stress components are computed from the wind vectors using a quadratic bulk formula with a constant drag coefficient of 1.4×10^{-3}. The ice velocity is not taken into account in the parameterization, so that the stresses can be used in both ice-covered and ice-free areas as a proxy for wind components. For experiments JRA and NCEP, within the ice pack, the differences in total ice concentration change with respect to DFS are explained by the fact that all experiments reach a concentration close to 1 in winter, while starting from distinct summer minima. Along the ice edge, the differences in concentration trends between March and August perfectly match the differences in ice concentration in September (Fig. 3).

As seen in Fig. 5, the lower concentrations in JRA compared to DFS along the sea ice edge in the Bellingshausen Sea mostly arise from reduced thermodynamic growth,

Table 3 Spatial averages of Antarctic sea ice concentration budgets derived from online model diagnostics (Figs. 5, 8), forcing air temperatures (Fig. 6) and wind stresses over ice (Figs. 7, 9), over March–August (MAMJJA) and October–January (ONDJ) 1985–2014

Experiment	TOT (10^{-3} day^{-1})	DYN (10^{-3} day^{-1})	THD (10^{-3} day^{-1})	Temperature (°C)	Wind stress (N m^{-2})
Interior—MAMJJA					
DFS	4.2	− 8.5	12.6	− 12.8	0.064
JRA	4.5 (+ 0.4)	− 10.5 (− 2.1)	15.0 (+ 2.4)	− 14.5 (− 1.7)	0.081 (+ 0.017)
NCEP	4.0 (− 0.2)	− 6.4 (+ 2.1)	10.4 (− 2.3)	− 15.8 (− 3.0)	0.054 (− 0.010)
Coast—MAMJJA					
DFS	3.3	− 39.9	43.2	− 15.0	0.081
JRA	3.1 (− 0.2)	− 57.6 (− 17.8)	60.7 (+ 17.5)	− 17.7 (− 2.6)	0.128 (+ 0.047)
NCEP	2.1 (− 1.2)	− 47.0 (− 7.1)	49.1 (+ 5.9)	− 19.6 (− 4.6)	0.095 (+ 0.014)
Interior—ONDJ					
DFS	− 6.2	− 4.6	− 1.6	− 5.7	0.046
JRA	− 7.0 (− 0.8)	− 5.2 (− 0.6)	− 1.8 (− 0.2)	− 5.6 (+ 0.0)	0.057 (+ 0.011)
NCEP	− 5.7 (+ 0.5)	− 3.3 (+ 1.3)	− 2.4 (− 0.8)	− 5.2 (+ 0.5)	0.034 (− 0.012)

TOT, DYN and THD stand for the total concentration change, its dynamic part and its thermodynamic part, respectively. The spatial averaging is computed over an interior domain delineated on the upper left panel of Fig. 5, and over a coastal domain corresponding to the grid cells located at less than 25 km of the coastline (usually just one cell). The numbers in parentheses correspond to the differences with respect to DFS

itself caused by slightly higher temperatures in this particular area during the ice expansion season (Fig. 6). Within the ice pack, since winter concentrations are always close to 1 in the model, the changes in the dynamics likely drive those in thermodynamics. Relative to DFS, stronger northeasterly winds along the coast of East Antarctica in JRA (Fig. 7) cause an increased dynamic reduction of the ice concentration (and an associated enhanced thermodynamic expansion) in a very narrow band along the continent. This band is barely visible in Fig. 5, but the effect is clear in the coastal averages listed in Table 3. Furthermore, this effect is reversed in a broader band further offshore. In the rest of the Antarctic sea ice zone, compensations exist between more negative dynamic trends and more positive thermodynamic trends. The faster drift in JRA is probably responsible for the larger dynamic reductions of ice concentrations.

Similar compensations exist for experiment NCEP compared to DFS, opposite in sign and stronger in magnitude (Fig. 5). Because of weaker winds, the sea ice cover is less dynamic in NCEP, which creates less open waters and thereby reduces the freezing rates in most regions in spite of much lower temperatures (Fig. 6). The signature of stronger coastal offshore winds is apparent too (Table 3). Along the ice edge, dynamic processes seem responsible for the larger ice extent between 90 to 180°E in NCEP. Winds indeed have a stronger northward component in this area (Fig. 7), favoring the advection of ice towards lower latitudes. Around West Antarctica, the difference pattern at the ice edge between DFS and NCEP is consistent with the one caused by changes in the Southern Annular Mode (SAM). Positive phases of this mode of atmospheric variability are associated with stronger westerlies around Antarctica and with a deeper Amundsen Sea Low (ASL). This deepening results in a dipolar regional sea ice response with little effects on the total extent (e.g., Lefebvre et al. 2004; Lefebvre and Goosse 2005; Turner et al. 2016). In the Ross and Amundsen sectors, stronger cold southerly winds lead to ice expansion in this area, from both dynamic and thermodynamic processes. On the eastern flank of the ASL, in the Bellingshausen and Weddell seas, the westerlies are deflected southeastwards, advecting warm air and compacting the ice cover around the Antarctic Peninsula. Our results, showing weaker westerlies and weaker southerly winds in the Ross Sea in NCEP (Fig. 7), point towards a difference between NCEP and DFS that has an effect similar to that of a negative phase of the SAM. The diagnostics in Fig. 5 further indicate that a combination of both dynamics and thermodynamics is needed to explain the ice concentration differences in the Ross, Amundsen and Bellingshausen sectors.

As mentioned above, the sea ice concentration budget based on the model diagnostics can also be examined in summer. The results are displayed in Fig. 8. The average is computed over the melting season going from October to January. In DFS, at the position of the maximum sea ice edge, the increase in concentration induced by dynamics is canceled by intense melting, as in winter. Within the ice zone, dynamic and thermodynamic contributions are both negative (Table 3), except along the coasts where freezing still occurs on average during this period.

The differences between the experiments can be linked to the differences in summer air temperatures (Fig. 6) and wind stresses (Fig. 9). Along the winter ice edge, the patterns of difference in total concentration changes directly reflect the distinct maximum extents in each simulation. Indeed, areas with larger September sea ice concentrations compared to DFS have a more negative total concentration change, and

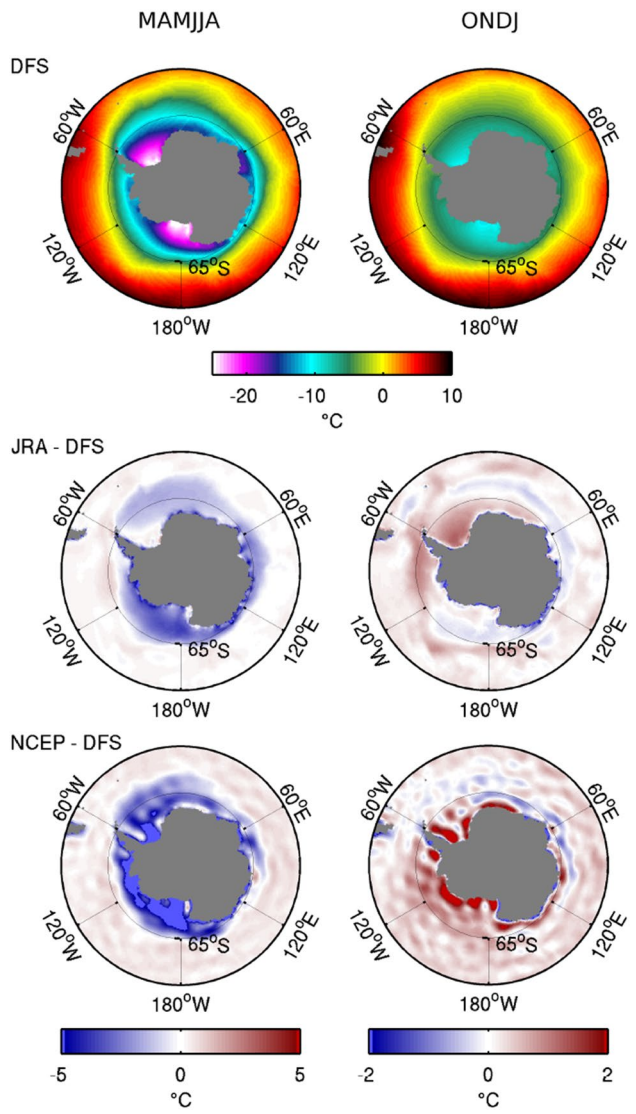

Fig. 6 Air temperatures in the atmospheric reanalyses used to drive the ocean–sea ice model, averaged over March–August (MAMJJA, left) and October–January (ONDJ, right) 1985–2014, for DFS and differences JRA-DFS and NCEP-DFS

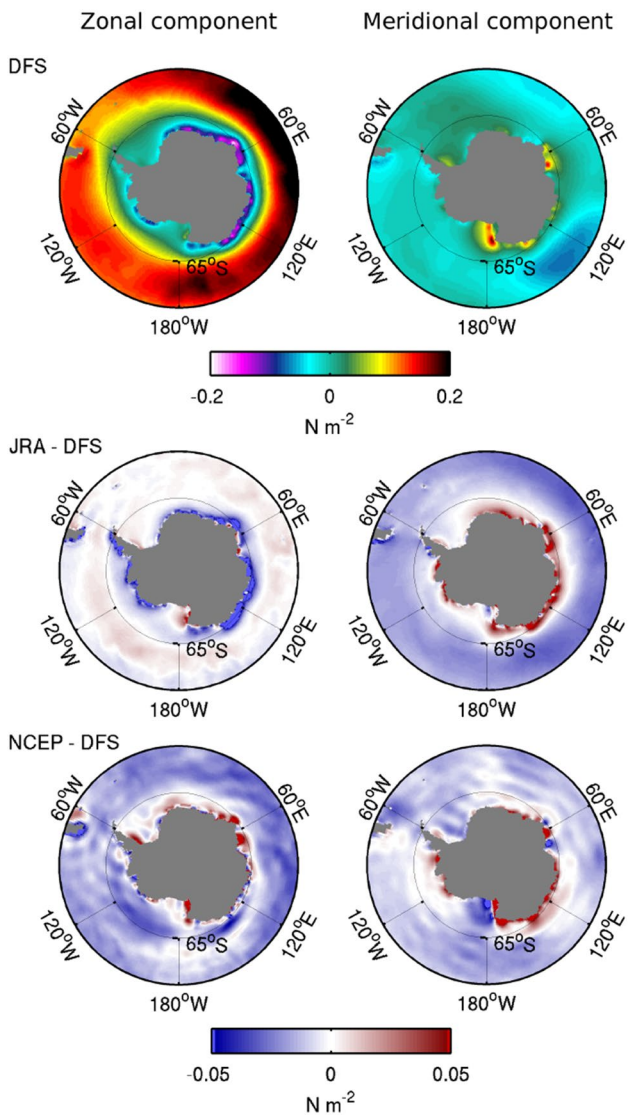

Fig. 7 Zonal (left) and meridional (right) components of the wind stress over ice, averaged over March–August 1985–2014, in experiment DFS and differences JRA-DFS and NCEP-DFS

conversely, since these areas become ice-free in all simulations at the end of the melting season. On the other hand, in interior sectors southward of the winter sea ice edge, they are indicative of the processes by which each experiment reaches its minimum extent.

In JRA, the larger summer ice losses can be attributed to increased local ice melt, corresponding to more negative thermodynamic concentration trends. The differences with respect to DFS are the largest in regions centered around the Greenwich meridian. They appear to be caused by more elevated temperatures in this area. In NCEP, higher summertime temperatures increase the thermodynamic sea ice losses in most interior sectors but the Weddell Sea. This is balanced by reduced dynamic decreases of the ice concentration (Table 3). In the Weddell Sea, the larger sea ice extent seems to be the result of thermodynamic processes, which however cannot be explained by temperature differences. Thicker ice in NCEP compared to DFS (see Sect. 4.5) might be the reason why the ice retreat is slower in this region. An examination of the ITD in a box located between 20 and 50°W and 64 and 69°S shows that 49 % (76 %) of the ice lies in the first two categories (i.e. with thicknesses below 1.13 m) in NCEP (DFS). The decrease in ice concentration for a given amount of basal melting is therefore more limited in NCEP compared to DFS. Finally, in the coastal area close to 45° E, dynamics are dominant in the ice concentration budget, with weaker easterly winds reducing the offshore export of ice there.

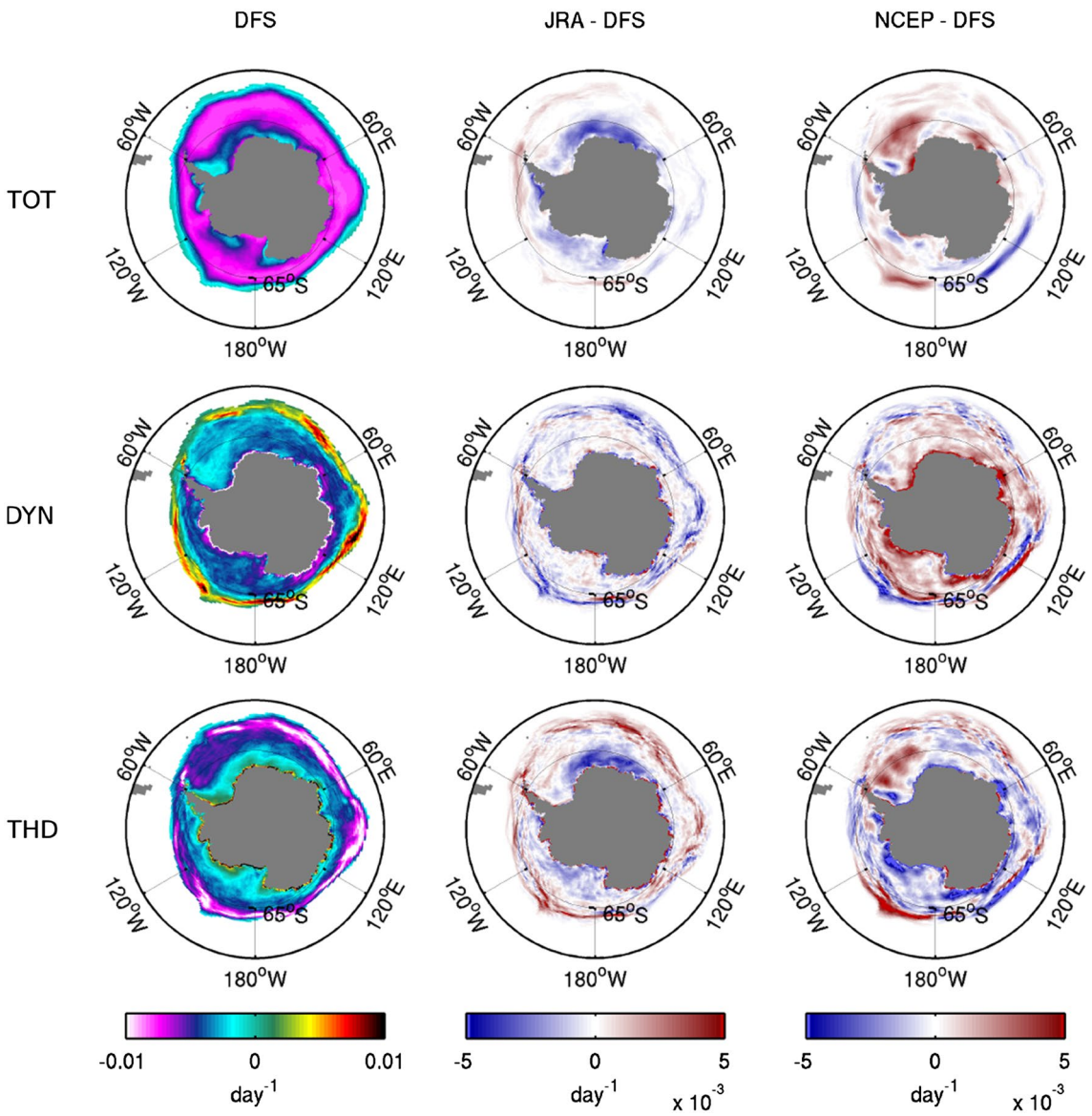

Fig. 8 Antarctic sea ice concentration budgets derived from online model diagnostics, averaged over October–January 1985–2014, in experiment DFS and differences JRA-DFS and NCEP-DFS. TOT, DYN and THD stand for the total concentration change, its dynamic part and its thermodynamic part, respectively. In the difference panels, blue (red) areas indicate stronger (weaker) ice concentration losses

Our results show that the differences in summer ice loss between the experiments are mostly explained by thermodynamic processes. In that respect, they are in line with those of Holland and Kimura (2016) based on observations, who had demonstrated the high importance of melt in the spring sea ice retreat.

4.4 Comparison with observed sea ice concentration budget

In the previous section, we have utilized the ice concentration budget derived from online diagnostics to examine in detail the changes between the experiments with different atmospheric forcings. Here, we apply the budget proposed by Holland and Kwok (2012) to compare the wintertime expansion of sea ice in simulations with observations. Although the main principle is similar, the decomposition of the ice concentration changes differs.

Following Holland and Kwok (2012), the evolution of the ice concentration A can be written as:

$$\frac{\partial A}{\partial t} = -\mathbf{u} \cdot \nabla A - A \nabla \cdot \mathbf{u} + (f - r) \tag{1}$$

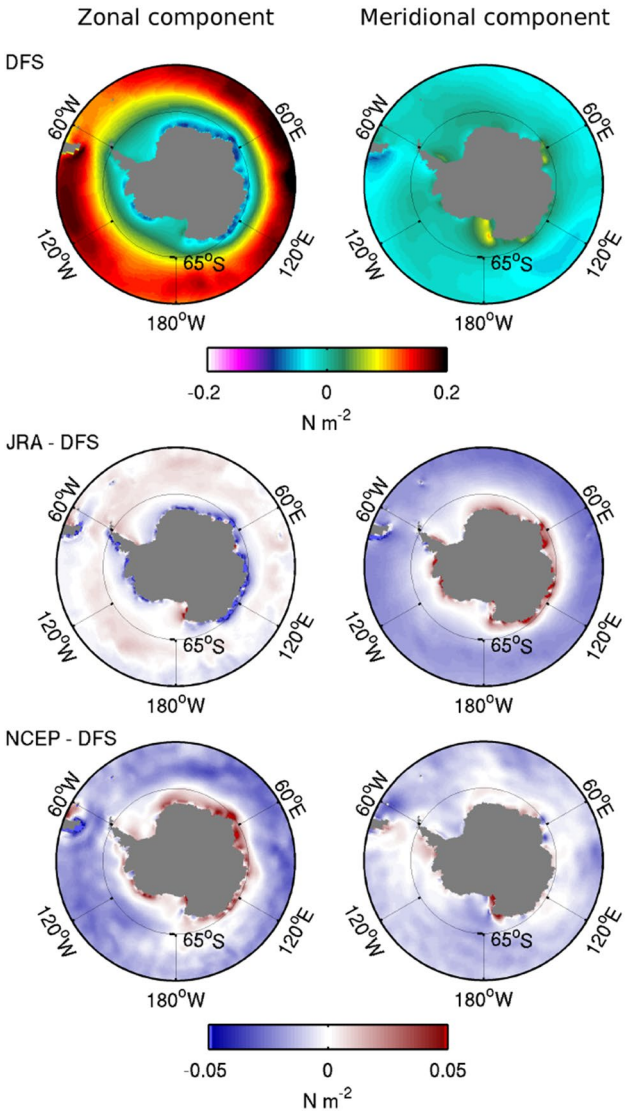

Fig. 9 Zonal (left) and meridional (right) components of the wind stress over ice, averaged over October–January 1985–2014, in experiment DFS and differences JRA-DFS and NCEP-DFS

where **u** is the ice velocity, f the change in concentration from freezing or melting, and r the one induced by mechanical redistribution processes such as rafting and ridging. These processes thicken the ice at the expense of its area. The above equation separates the total change in sea ice concentration into the three terms in the right-hand side: the advection, the divergence, and the thermodynamics and mechanical redistribution. The observed budget is derived from daily satellite products for A and **u**, with the last term being computed as a residual, and is integrated over the period from April to October between 1992 and 2010. The simulated budget is calculated in a consistent way from model outputs. More details on the computations can be found in Lecomte et al. (2016).

It must be noted that the large uncertainties in satellite ice motion products (illustrated by the differences between the Kimura et al. (2013) and Fowler et al. (2013) datasets in Fig. 4 for instance) do have a substantial impact on the observed ice concentration budget. Using the ice speeds from Kimura et al. (2013) in the budget computation gives results that are in good agreement with those of Holland and Kwok (2012), which are based on an ice motion dataset that is not yet publicly available (Holland and Kimura 2016). By contrast, an analysis based on the relatively slow ice speeds of Fowler et al. (2013) would give results that are significantly different (Lecomte et al. 2016). Since the Fowler et al. (2013) data have been reported to be too slow (Heil et al. 2001), we have greater confidence in the budget computed by Holland and Kwok (2012). These uncertainties should nonetheless be kept in mind in the following analysis.

The observed budget presented in Fig. 10 confirms that freezing (included in the residual component) within the ice pack is mostly driven by its divergence, and that the advection of ice is compensated by melt at lower latitudes. Qualitatively, these features are also found in the concentration budget of experiment DFS. The total change in concentration is however larger at the ice cover periphery in DFS than in the observations, which is consistent with the overestimation of the winter extent in this simulation. Part of this bias can be attributed to an excessive advection of ice towards lower latitudes along the ice edge, which is only partly counterbalanced by thermodynamic melt. While the model overestimates the ice divergence in a narrow band along the coast of East Antarctica, it presents three large areas of spurious convergence centered around 30°E, 120°E and 100°W. A lack of divergence and a too strong advection are visible in forced and coupled simulations with other models as well (Uotila et al. 2014; Lecomte et al. 2016).

In spite of substantial differences in ice speed, the sea ice concentration budgets for JRA and NCEP are similar to the one of experiment DFS, and the inconsistencies with the observed budget described above are also valid for these simulations (not shown). In particular, the slower ice drift in NCEP, which seems to agree better with observational estimates than DFS, is not clearly associated with an improved representation of the advection term. This suggests that the positive bias in advection in the model might be caused, at least partly, by the overall overestimation of ice concentration which is present in all simulations. Additionally, the lack of divergence in the central ice pack is found in all experiments. It is largest in JRA, even though this forcing yields the highest sea ice speeds. Table 4 lists root-mean-square errors between observed and simulated ice concentration budgets. Although the errors for the three budget components are slightly lower for DFS, they remain large in all cases and are only moderately influenced by changes of atmospheric forcing. By contrast, the impacts of using

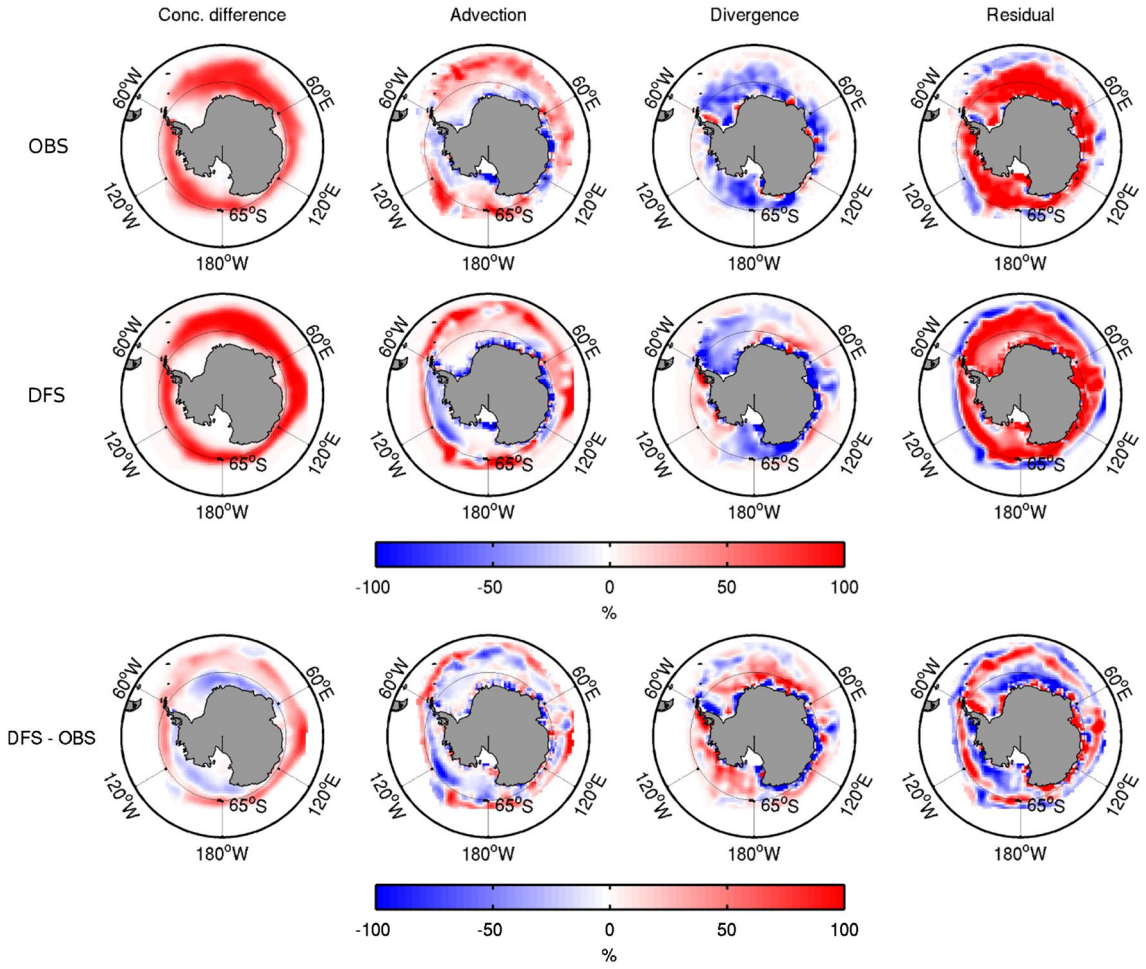

Fig. 10 Antarctic sea ice concentration budget, averaged over April–October 1992–2010, from the observational data of Holland and Kwok (2012) (top) and as computed from experiment DFS (middle). The mean April–October ice concentration difference ($\overline{\int \frac{\partial A}{\partial t} dt}$) displayed on the left is split into changes due to advection ($-\overline{\int \mathbf{u} \cdot \nabla A \, dt}$; red (blue) represents a local import (export) of sea ice), divergence ($-\overline{\int A \nabla \cdot \mathbf{u} \, dt}$; red (blue) represents a convergence and closing (divergence and opening) of the sea ice cover) and residual thermodynamic changes and mechanical redistribution ($\overline{\int (f - r) \, dt}$; red (blue) represents an increase (decrease) in sea ice concentration related to these processes). The difference between DFS and the observations is also shown (bottom)

Table 4 Root-mean-square error between observed (Holland and Kwok 2012) and simulated sea ice concentration budgets in the different experiments, over April–October 1992–2010

Experiment	DFS	JRA	NCEP
Conc. difference (%)	24	21	24
Advection (%)	38	46	49
Divergence (%)	66	85	75
Residual (%)	65	76	73

different models were larger in the studies of Uotila et al. (2014) and Lecomte et al. (2016). Hence, this suggests that factors other than the forcing, such as the model physics, may have a greater importance for the simulated sea ice concentration budget in winter.

4.5 Sea ice thickness and volume

So far, we have analyzed the effects of the atmospheric forcings on the horizontal distribution of sea ice. Their impacts on the ice thickness are also critical, since the changes in sea ice volume determine the thermohaline fluxes to the ocean. The differences between the experiments that we describe in this section actually result in differences in salt and freshwater sea ice-ocean exchanges (not shown). The oceanic heat flux to the ice base differ by as much as 10 W m^{-2} between the simulations during the winter season. Mixed layer depths show some sensitivity to the atmospheric forcing as well, especially along the continent. Links between the changes in these diagnostics are however not clear, and they do not explain the simulated ice differences in a convincing way.

We conclude that, in our experiments, although the forcing does induce changes in the ocean structure, the impacts of these changes on the simulated sea ice can be considered second order effects compared to the direct influence of the forcing on the ice.

As seen in Fig. 1, large differences exist between the experiments with the three forcing sets in terms of total sea ice volume. At the seasonal maximum in October, JRA (DFS) has the highest (lowest) volume at 20×10^3 km^3 (around 16×10^3 km^3). The larger volume in JRA compared to DFS can be attributed to lower air temperatures (Fig. 6). In February, the JRA volume is 0.5×10^3 km^3 smaller than DFS, which is consistent with higher summer temperatures and with a smaller minimum extent. The behavior of experiment NCEP cannot be completely explained by the forcing temperatures. In spite of being the coldest during the wintertime, locally more than 5 °C colder than DFS, its maximum ice volume is smaller than JRA, with a value around 17×10^3 km^3. The slow dynamics of the NCEP sea ice, which have visible impacts on the winter ice concentration budget, also limit the volume of ice produced during the cold season. Nevertheless, the maximum volume is around 2×10^3 km^3 larger than in DFS, and it remains so during the whole year, notwithstanding higher summer temperatures.

For comparison, the total Antarctic sea ice volume in a reanalysis (Massonnet et al. 2013) and in satellite estimates (Kurtz and Markus 2012) varies between 2 and 10×10^3 km^3 and 3 and 11×10^3 km^3, respectively. Our model thus seems to significantly overestimate the winter volume, regardless of the forcing used. In terms of long-term evolution, all of our simulations appear compatible with the trend of $+ 36 \pm 34$ km^3 year^{-1} obtained for the period 1980–2008 by Massonnet et al. (2013).

The spatial distributions of winter sea ice thickness are shown in Fig. 11. As expected for the differences in volume, ice is thicker almost everywhere in JRA and NCEP compared to DFS. On average in the areas where the sea ice concentration exceeds 15 %, the September thickness is 0.86, 0.79 and 0.69 m in JRA, NCEP and DFS, respectively. The depth of snow on top of the ice differs between the simulations (not shown), but it does not explain the thickness difference patterns, neither through an insulating effect that would reduce the ice thickening, nor through the formation of snow ice that would enhance it. More generally, the differences in thickness between the experiments cannot be explained by changes in just one of the various processes through which new ice volume is formed, namely freezing in open waters, bottom growth, creation of porous ridges and snow ice formation. They rather result from a combination of simultaneous changes in several of these processes.

Nonetheless, a striking difference between the DFS/JRA and NCEP experiments is the position of the ice thickness maximum in the Weddell Sea. In DFS and JRA, the thickest

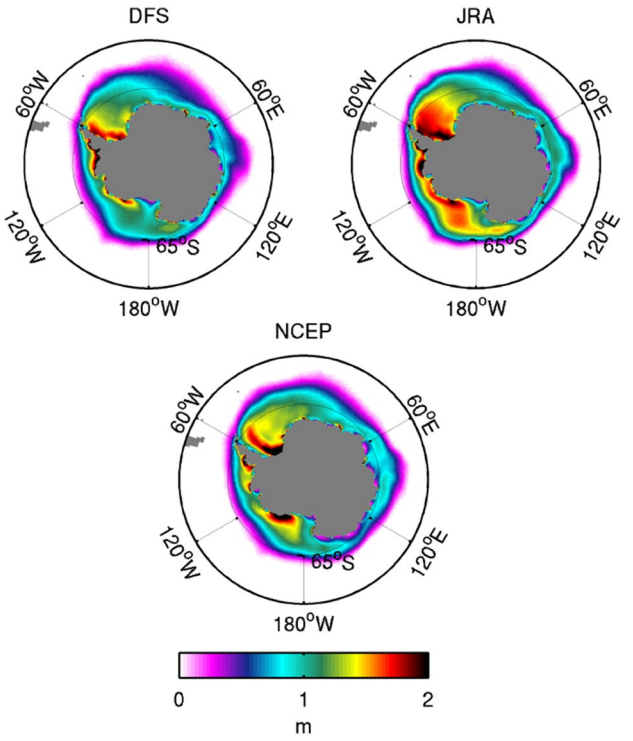

Fig. 11 September sea ice thicknesses, averaged over 1985–2014, in the different experiments. The average sea ice thickness over the whole grid cell, or the sea ice volume per unit area, is actually plotted. Ice 1 m thick at 50 % concentration would hence appear as 0.5 m thick in the figure

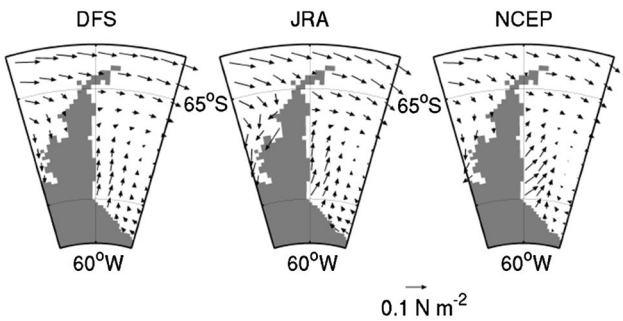

Fig. 12 September wind stresses over ice around the Antarctic Peninsula, averaged over 1985–2014, in the different experiments. Vectors are drawn at every four grid points

ice is found along the Ronne Ice Shelf and along the coast of the Antarctic Peninsula, with only the southwestern corner of the Weddell Sea showing thinner ice because of strong offshore winds (e.g., Haid et al. 2015). In experiment NCEP, thick ice is pushed away from the peninsula by winds with a spurious westerly component (Fig. 12), blowing from March to October. This gives rise to an ice thickness pattern that is not consistent with observations (Timmermann et al. 2004; Worby et al. 2008). Simulated

winds on the eastern side of the Antarctic Peninsula indeed clearly depend on the representation of its orography, which is poor in NCEP because of its low resolution. On the contrary, the local southerly winds resulting from the blocking effect of the peninsula mountain range, known as barrier winds, are more accurately resolved in higher resolution forcings such as DFS and JRA (Stössel et al. 2011; Haid et al. 2015). These forcings therefore provide a notable improvement in the simulated ice thickness patterns in the Weddell Sea, although the thickest ice should extend even further north to be in line with observations from upward looking sonars (Timmermann et al. 2005).

5 Conclusions

The objective of this study was to examine how biases in Antarctic sea ice simulations relate to atmospheric forcing uncertainties. To this end, the ocean-sea ice model NEMO-LIM has been driven by forcing sets derived from three atmospheric reanalyses. While DFS and JRA share several similarities, we also used the NCEP reanalysis, which has a much coarser horizontal resolution and which is used with a different forcing formulation. The three products differ substantially from one another in the Southern Ocean area in terms of both dynamics and thermodynamics, as seen from the large differences in their surface winds and temperatures.

Our results suggest that forcing adjustments suffice in improving some of the model biases, while solving other issues in the representation of the Antarctic sea ice would require further changes to the modeling system. More specifically, in NEMO-LIM, the atmospheric forcing has a strong influence on:

- the speed of the summertime sea ice retreat, the minimum ice extent and the spatial distribution of ice at the minimum extent;
- the sea ice drift speeds, which clearly depend on the winds used to drive the model;
- the total sea ice volume and the spatial patterns of ice thickness.

We note that the high ice thickness sensitivity is in line with the results obtained by Hunke and Holland (2007) and Lindsay et al. (2014) for the Arctic. On the contrary, the atmospheric forcing has little impact on:

- the maximum sea ice extent, although there are small regional changes in the position of the winter ice edge;
- the winter sea ice concentrations within the ice pack, which are consistently overestimated compared to observations.

The larger model sensitivity to the atmospheric forcing during the melt season than during the growth season (especially in terms of ice concentration and extent) contrasts with the results of Schroeter et al. (2017), who showed that the atmospheric influence on Antarctic sea ice is stronger during its expansion than during its retreat. The fact that they examined interannual variability in coupled models, while we focus on the mean state in a forced model, might explain why we obtain distinct conclusions.

The ice distribution at the February minimum and the seasonal cycle of ice speeds are best represented with JRA and NCEP, respectively. Nevertheless, DFS provides the smallest overestimation of the winter ice volume with respect to available estimates, a realistic ice thickness pattern close to the Antarctic Peninsula and a slightly better agreement with the observed ice concentration budget of Holland and Kwok (2012).

Furthermore, the examination of sea ice concentration budgets has led to two outcomes. First, online diagnostics have allowed a deeper understanding of the processes leading to differences between the experiments. During the ice expansion period and in the ice pack interior, thermodynamics tend to compensate the changes that would be caused by dynamics. Along the ice edge, processes of both types are needed to explain the regional differences between the simulations. The melting season is characterized by a greater role of thermodynamics. Second, we have confirmed the results of Uotila et al. (2014), namely that current models show significant deviations from the observed ice concentration budget. Large compensations exist between the different terms, and our work indicates that the atmospheric forcing has a limited impact on these biases.

Lecomte et al. (2016) suggested analyzing Antarctic sea ice concentration budgets for simulations using different atmospheric forcings or different model physics. We hypothesize that the importance of physics might be greater than previously acknowledged. Indeed, although earlier studies concluded that upgrading a sea ice model do not enhance its skill in the Antarctic, large changes are actually induced by such modifications (Massonnet et al. 2011; Uotila et al. 2017). The lack of improvement in skill might be the result of focusing model developments on processes having more impacts on ice types encountered in the Arctic. The formation of frazil, ice pancakes and snow ice, for instance, are more prevalent in the Southern Ocean and are currently not adequately represented in models. Among the most promising prospects for a better simulation of ice dynamics, the rheology presumably comes first. Recently developed sea ice rheologies are more skillful in representing ice deformation (e.g., Tsamados et al. 2013; Dansereau et al. 2016). New parameterizations of the drag coefficients based on the ice morphology (e.g., Lüpkes et al. 2012; Tsamados et al. 2014) could then be exploited to their best advantage to improve

the simulated ice drift, which would impact the associated terms of the ice concentration budget.

Finally, the importance of the performance of the ocean model in dictating the evolution of Antarctic sea ice cannot be understated. This is exemplified by the discussion of the effects of vertical resolution changes in the "Appendix". In addition, we have noticed that the atmospheric forcing has an influence on the under-ice ocean properties. Although these oceanic changes appear as second order processes as far as the sea ice simulation is concerned, a targeted examination of the forcing effects on the Southern Ocean structure and dynamics would be valuable.

Acknowledgements We thank two anonymous reviewers for their valuable comments on the original manuscript. H. G. and O. L. are respectively Research Director and Postdoctoral Researcher with the Fonds de la Recherche Scientifique (F.R.S.-FNRS/Belgium). This work was supported by the F.R.S.-FNRS research project "Amélioration de la représentation de la glace de mer antarctique dans les modèles climatiques grâce à? une meilleure compréhension des processus gouvernant son état moyen et sa variabilité", under grant agreement T.0007.14. Computational resources have been provided by the supercomputing facilities of the Université catholique de Louvain (CISM/UCL) and the Consortium des Equipements de Calcul Intensif en Fédération Wallonie Bruxelles (CECI) funded by the F.R.S.-FNRS under convention 2.5020.11.

Appendix: Ocean vertical resolution

As noted in Sect. 2.3, the vertical resolution of the ocean in the present model configuration is higher than in most previous studies. Usually, the ORCA1 grid has indeed been used with 46 layers, whose thicknesses range from 6 m at the surface to 20 at 100 m depth, and to 250 m for the bottommost layer. For comparison, at the same depths, the layer thicknesses in the eORCA1 grid with 75 levels are 1, 10 and 200 m. In this appendix, we examine the effects of this change. To this end, an additional experiment is conducted, named LVR. It is the exact equivalent of DFS except for its lower vertical resolution.

As seen in Fig. 1, changing the ocean model vertical resolution has a negligible effect on the summer Antarctic sea ice extent. Regional differences in ice concentration between experiments LVR and DFS actually exist during the melting season, but they are small and they compensate each other in the total sea ice extent. By contrast, the latter is clearly reduced during the expansion period, by up to 2×10^6 km^2, even though the ocean-sea ice model is used in forced mode. The strongest decrease in ice concentration takes place close to 130°W (Fig. 13), a region where DFS already underestimated the sea ice area compared to observations. Furthermore, concentrations are lower inside the ice pack in LVR, but they remain nevertheless higher than satellite estimates.

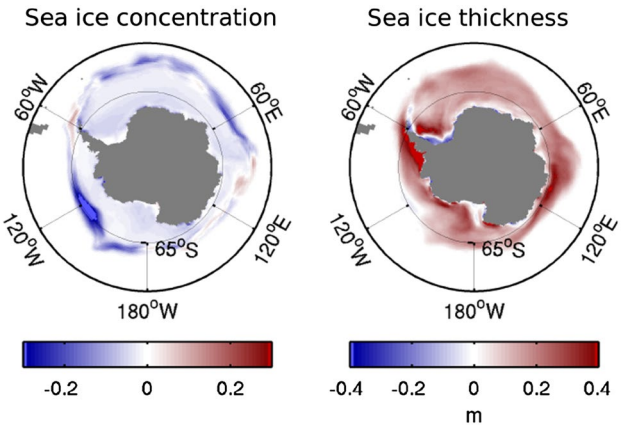

Fig. 13 Differences in September sea ice concentration (left) and thickness (right) between experiments LVR and DFS (LVR-DFS), averaged over 1985–2014

In spite of a smaller extent, the sea ice volume in experiment LVR is larger than in DFS (Fig. 1). The difference peaks at 3×10^3 km^3 in October, and a fraction of it persists throughout the year. It is related to an ice thickening of up to a few tens of centimeters in LVR, in most regions but the southern and southwestern parts of the Weddell Sea, where a slight thinning occurs (Fig. 13).

These changes between the simulations with different vertical resolutions are explained by how the model handles new ice formation in open waters. In conditions of ice growth, the open water heat loss to the atmosphere is split into two parts (Barthélemy et al. 2016a). The first one is used to lower the temperature of the top oceanic grid cell to the freezing point. The remaining heat loss must then be compensated by latent heat released by seawater freezing, which is associated with expansion of ice in the open water fraction of the grid cell. The thickness of the first ocean layer being 1 m in DFS and 6 m in LVR, at equivalent ocean temperature, more energy is needed in LVR to cool the surface down to the freezing point, and less energy is left for sea ice formation in open waters. This is the reason why ice concentrations are lower in LVR than in DFS. The lesser contribution of thermodynamic processes to the expansion of sea ice in LVR is indeed visible in the winter ice concentration budget based on online model diagnostics (not shown).

Subsequently, convection due to surface cooling and brine rejection from ice growth will homogenize the winter mixed layer. Since a thicker ocean layer needed to be cooled in LVR to allow for ice formation in open waters, the temperature of the mixed layer will become lower in this simulation. This is visible in the mean August temperature profiles displayed in Fig. 14. Close to the surface and on average south of 65°S, LVR is about 0.05 °C colder than DFS, with a larger difference at greater depths. A lower sea surface temperature implies a smaller oceanic heat flux to the ice

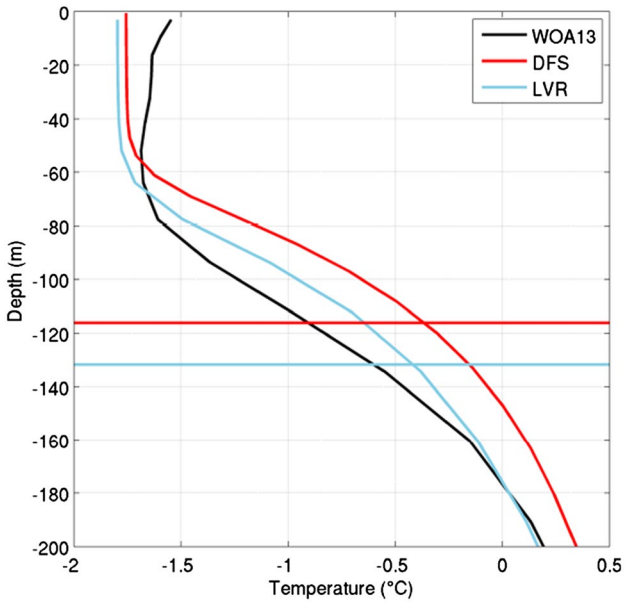

Fig. 14 August ocean temperature profiles, averaged over 1985–2014 and south of 65°S, in the WOA13 climatology (Locarnini et al. 2013) and in experiments DFS and LVR. The horizontal lines show the simulated mean mixed layer depths

base. In August, just before the sea ice maximum, the mean heat flux is reduced by half in the low resolution case (not shown). Differences of several tens of W m^{-2} occur along the ice edge, where the flux is the highest in DFS due to relatively warm waters. In turn, the decreased oceanic heat supply to the ice in LVR explains the increase in ice thickness in this experiment.

Finally, the simulated mixed layers are deeper in LVR, as a consequence of the surface cooling and of enhanced brine rejection linked to larger sea ice production. On average south of 65°S, the difference between the two simulations amounts to 15 m. While LVR appears to be in better agreement with WOA13 temperature profiles, the increase in mixed layer depth enhances the deep bias already present in DFS with respect to an observation-based climatology (Pellichero et al. 2017).

Based on this understanding of the first order effects of a reduced vertical resolution, we can re-examine the spatial patterns of changes in Fig. 13. The fact that sea ice is not thicker in LVR in the southern parts of the Weddell Sea can be explained by ocean temperatures close to the freezing point in that area, implying that the process described above does not play an active role there. By contrast, subsurface temperatures are the highest in the Amundsen Sea. In this region, the vertical mixing induced by new ice production at low resolution causes a upward heat transport which offsets the initial cooling. Higher surface temperatures decrease strongly the sea ice concentration and prevent the ice thickening visible elsewhere.

Depending on the variable considered, the best agreement with observations is provided by either DFS or LVR. More importantly, these results demonstrate that changing the vertical resolution of a model could require adjusting the treatment of some physical processes as well. The issue is similar to that of the increase in the horizontal resolution of ocean models, in which the eddy parameterizations must be adapted when the simulations become eddy-resolving (e.g., Iovino et al. 2016). In our case, it is not realistic that only the 1 m surface layer of the ocean is associated with new sea ice formation in DFS. In reality, turbulent mixing continuously mixes the upper water layer, over a thickness larger than than 1 m, thereby coupling it with the freezing taking place at the surface. Even if vertical mixing is realistically simulated, connections between the surface and the second ocean layer (and the deeper ones) can only occur at the model time step frequency. The results described above suggest that a more advanced representation of the formation of new ice in open waters (e.g., Wilchinsky et al. 2015; Barthélemy et al. 2016b) might help reduce the modeled winter sea ice concentrations.

References

Barthélemy A, Fichefet T, Goosse H (2016) Spatial heterogeneity of ocean surface boundary conditions under sea ice. Ocean Modell 102:82–98. doi:10.1016/j.ocemod.2016.05.003

Barthélemy A, Fichefet T, Goosse H, Madec G (2016) A multi-column vertical mixing scheme to parameterize the heterogeneity of oceanic conditions under sea ice. Ocean Modell 104:28–44. doi:10.1016/j.ocemod.2016.05.005

Berliand ME, Strokina TG (1980) Global distribution of the total amount of clouds (in Russian). Tech. rep., Hydrometeorological Publishing House, Leningrad

Blanke B, Delecluse P (1993) Variability of the tropical Atlantic ocean simulated by a general circulation model with two different mixed-layer physics. J Phys Oceanogr 23(7):1363–1388. doi:10.1175/1520-0485(1993)023<1363:VOTTAO>2.0.CO;2

Bouillon S, Fichefet T, Legat V, Madec G (2013) The elastic-viscous-plastic method revisited. Ocean Modell 71:2–12. doi:10.1016/j.ocemod.2013.05.013

Bracegirdle TJ, Stephenson DB, Turner J, Phillips T (2015) The importance of sea ice area biases in 21st century multimodel projections of Antarctic temperature and precipitation. Geophys Res Lett 42(24):10,832–10,839. doi:10.1002/2015GL067055

Brodeau L, Barnier B, Treguier AM, Penduff T, Gulev S (2010) An ERA40-based atmospheric forcing for global ocean circulation models. Ocean Modell 31(3–4):88–104. doi:10.1016/j.ocemod.2009.10.005

Bromwich DH, Fogt RL, Hodges KI, Walsh JE (2007) A tropospheric assessment of the ERA-40, NCEP, and JRA-25 global reanalyses in the polar regions. J Geophys Res 112(D10):D10,111. doi:10.1029/2006JD007859

Cavalieri DJ, Parkinson CL, Gloersen P, Zwally H (1996) Sea Ice Concentrations from Nimbus-7 SMMR and DMSP SSM/I-SSMIS Passive Microwave Data. [1979–2010], NASA National Snow and Ice Data Center Distributed Active Archive Center, Boulder, Colorado, USA, doi:10.5067/8GQ8LZQVL0VL

Chaudhuri AH, Ponte RM, Forget G (2016) Impact of uncertainties in atmospheric boundary conditions on ocean model solutions. Ocean Modell 100:96–108. doi:10.1016/j.ocemod.2016.02.003

Dai A, Trenberth KE (2002) Estimates of freshwater discharge from continents: latitudinal and seasonal variations. J Hydrometeor 3(6):660–687. doi:10.1175/1525-7541(2002)003<0660:EOFDFC>2.0.CO;2

Dansereau V, Weiss J, Saramito P, Lattes P (2016) A Maxwell elasto-brittle rheology for sea ice modelling. Cryosphere 10(3):1339–1359. doi:10.5194/tc-10-1339-2016

Depoorter MA, Bamber JL, Griggs JA, Lenaerts JTM, Ligtenberg SRM, van den Broeke MR, Moholdt G (2013) Calving fluxes and basal melt rates of Antarctic ice shelves. Nature 502(7469):89–92. doi:10.1038/nature12567

Dussin R, Barnier B, Brodeau L, Molines JM (2016) The making of the DRAKKAR Forcing Set DFS5. Drakkar/myocean report 01-04-16, Laboratoire de Glaciologie et de Géophysique de l'Environnement, Université de Grenoble, Grenoble, France

EUMETSAT (2015) Global sea ice concentration reprocessing dataset 1978-2015 (v1.2). http://osisaf.met.no, Ocean and Sea Ice Satelitte Application Facility, Norwegian and Danish Meteorological Institutes

Fetterer F, Knowles K, Meier W, Savoie M (2016) Sea ice index, version 2. Updated daily. National Snow and Ice Data Center, Boulder, Colorado. doi:10.7265/N5736NV7

Fowler C, Maslanik J, Emery W, Tschudi M (2013) Polar Pathfinder Daily 25 km EASE-grid sea ice motion vectors. version 2. [2003–2010]. National Snow and Ice Data Center, Boulder. doi:10.5067/O57VAIT2AYYY

Gent PR, Mcwilliams JC (1990) isopycnal mixing in ocean circulation models. J Phys Oceanogr 20(1):150–155. doi:10.1175/1520-0485(1990)020<0150:IMIOCM>2.0.CO;2

Goosse H (1997) Modelling the large-scale behaviour of the coupled ocean-sea-ice system. PhD thesis, Université catholique de Louvain

Haid V, Timmermann R, Ebner L, Heinemann G (2015) Atmospheric forcing of coastal polynyas in the south-western Weddell Sea. Antarct Sci 27(4):388–402. doi:10.1017/S0954102014000893

Heil P, Fowler CW, Maslanik JA, Emery WJ, Allison I (2001) A comparison of East Antarctic sea-ice motion derived using drifting buoys and remote sensing. Ann Glaciol 33(1):139–144. doi:10.3189/172756401781818374

Hobbs WR, Massom R, Stammerjohn S, Reid P, Williams G, Meier W (2016) A review of recent changes in Southern Ocean sea ice, their drivers and forcings. Glob Planet Change 143:228–250. doi:10.1016/j.gloplacha.2016.06.008

Holland PR, Kimura N (2016) Observed concentration budgets of Arctic and Antarctic sea ice. J Clim 29(14):5241–5249. doi:10.1175/JCLI-D-16-0121.1

Holland PR, Kwok R (2012) Wind-driven trends in Antarctic sea-ice drift. Nat Geosci 5(12):872–875. doi:10.1038/ngeo1627

Hunke EC, Holland MM (2007) Global atmospheric forcing data for Arctic ice-ocean modeling. J Geophys Res 112(C4):1–13. doi:10.1029/2006JC003640

Iovino D, Masina S, Storto A, Cipollone A, Stepanov VN (2016) A 1/16° eddying simulation of the global NEMO sea-ice-ocean system. Geosci Model Dev 9(8):2665–2684. doi:10.5194/gmd-9-2665-2016

Ivanova N, Pedersen LT, Tonboe RT, Kern S, Heygster G, Lavergne T, Sørensen A, Saldo R, Dybkjær G, Brucker L, Shokr M (2015) Inter-comparison and evaluation of sea ice algorithms: towards further identification of challenges and optimal approach using passive microwave observations. Cryosphere 9(5):1797–1817. doi:10.5194/tc-9-1797-2015

Jones RW, Renfrew IA, Orr A, Webber BGM, Holland DM, Lazzara MA (2016) Evaluation of four global reanalysis products using in situ observations in the Amundsen Sea Embayment, Antarctica. J Geophys Res Atmos 121(11):6240–6257. doi:10.1002/2015JD024680

Kalnay E, Kanamitsu M, Kistler R, Collins W, Deaven D, Gandin L, Iredell M, Saha S, White G, Woollen J, Zhu Y, Leetmaa A, Reynolds R, Chelliah M, Ebisuzaki W, Higgins W, Janowiak J, Mo KC, Ropelewski C, Wang J, Jenne R, Joseph D (1996) The NCEP/NCAR 40-Year Reanalysis Project. Bull Am Meteor Soc 77(3):437–471. doi:10.1175/1520-0477(1996)077<0437:TNYRP>2.0.CO;2

Kimura N, Nishimura A, Tanaka Y, Yamaguchi H (2013) Influence of winter sea ice motion on summer ice cover in the Arctic. Polar Res 32(20):193. doi:10.3402/polar.v32i0.20193

Kobayashi S, Ota Y, Harada Y, Ebita A, Moriya M, Onoda H, Onogi K, Kamahori H, Kobayashi C, Endo H, Miyaoka K, Takahashi K (2015) The JRA-55 Reanalysis: General Specifications and Basic Characteristics. J Meteorol Soc Jpn 93(1):5–48. doi:10.2151/jmsj.2015-001

Kurtz NT, Markus T (2012) Satellite observations of Antarctic sea ice thickness and volume. J Geophys Res 117(C8):C08,025. doi:10.1029/2012JC008141

Large WG, Yeager SG (2004) Diurnal to decadal global forcing for ocean and sea-ice models: The data sets and flux climatologies. Tech. rep., National Center for Atmospheric Research, Boulder

Lecomte O, Goosse H, Fichefet T, Holland P, Uotila P, Zunz V, Kimura N (2016) Impact of surface wind biases on the Antarctic sea ice concentration budget in climate models. Ocean Modell 105:60–70. doi:10.1016/j.ocemod.2016.08.001

Lefebvre W, Goosse H (2005) Influence of the Southern Annular Mode on the sea ice-ocean system: the role of the thermal and mechanical forcing. Ocean Sci 1(3):145–157. doi:10.5194/os-1-145-2005

Lefebvre W, Goosse H, Timmermann R, Fichefet T (2004) Influence of the Southern Annular Mode on the sea ice-ocean system. J Geophys Res 109(C9):1–12. doi:10.1029/2004JC002403

Lindsay R, Wensnahan M, Schweiger A, Zhang J (2014) Evaluation of seven different atmospheric reanalysis products in the Arctic. J Clim 27(7):2588–2606. doi:10.1175/JCLI-D-13-00014.1

Locarnini RA, Mishonov AV, Antonov JI, Boyer TP, Garcia HE, Baranova OK, Zweng MM, Paver CR, Reagan JR, Johnson DR, Hamilton M, Seidov D (2013) World Ocean Atlas 2013 Volume 1: Temperature. In: Levitus S (ed) mishonov technical ed., noaa atlas nesdis. National Centers for Environmental Information, p 73, 40

Lüpkes C, Gryanik VM, Hartmann J, Andreas EL (2012) A parametrization, based on sea ice morphology, of the neutral atmospheric drag coefficients for weather prediction and climate models. J Geophys Res 117(D13):D13,112. doi:10.1029/2012JD017630

Madec G (2008) NEMO ocean engine. Note du Pôle de modélisation 27. Institut Pierre-Simon Laplace, France, iSSN No 1288-1619

Madec G, Imbard M (1996) A global ocean mesh to overcome the North Pole singularity. Clim Dyn 12(6):381–388. doi:10.1007/BF00211684

Massonnet F, Fichefet T, Goosse H, Vancoppenolle M, Mathiot P, König Beatty C (2011) On the influence of model physics on simulations of Arctic and Antarctic sea ice. Cryosphere 5(3):687–699. doi:10.5194/tc-5-687-2011

Massonnet F, Mathiot P, Fichefet T, Goosse H, König Beatty C, Vancoppenolle M, Lavergne T (2013) A model reconstruction of the Antarctic sea ice thickness and volume changes over 1980–2008 using data assimilation. Ocean Modell 64:67–75. doi:10.1016/j.ocemod.2013.01.003

Merino N, Le Sommer J, Durand G, Jourdain NC, Madec G, Mathiot P, Tournadre J (2016) Antarctic icebergs melt over the Southern Ocean: climatology and impact on sea ice. Ocean Modell 104:99–110. doi:10.1016/j.ocemod.2016.05.001

Nihashi S, Ohshima KI (2015) Circumpolar mapping of antarctic coastal polynyas and landfast sea ice: relationship and variability. J Clim 28(9):3650–3670. doi:10.1175/JCLI-D-14-00369.1

Pellichero V, Sallée JB, Schmidtko S, Roquet F, Charrassin JB (2017) The ocean mixed layer under Southern Ocean sea-ice: seasonal cycle and forcing. J Geophys Res Oceans 122(2):1608–1633. doi :10.1002/2016JC011970

Rousset C, Vancoppenolle M, Madec G, Fichefet T, Flavoni S, Barthélemy A, Benshila R, Chanut J, Levy C, Masson S, Vivier F (2015) The Louvain-La-Neuve sea ice model LIM3.6: global and regional capabilities. Geosci Model Dev 8(10):2991–3005. doi:10.5194/gmd-8-2991-2015

Schroeter S, Hobbs W, Bindoff NL (2017) Interactions between Antarctic sea ice and large-scale atmospheric modes in CMIP5 models. Cryosphere 11(2):789–803. doi:10.5194/tc-11-789-2017

Shu Q, Song Z, Qiao F (2015) Assessment of sea ice simulations in the CMIP5 models. Cryosphere 9(1):399–409. doi:10.5194/tc-9-399-2015

Stössel A, Zhang Z, Vihma T (2011) The effect of alternative real-time wind forcing on Southern Ocean sea ice simulations. J Geophys Res 116(C11):1–19. doi:10.1029/2011JC007328

Timmermann R, Worby A, Goosse H, Fichefet T (2004) Utilizing the ASPeCt sea ice thickness data set to evaluate a global coupled sea ice-ocean model. J Geophys Res 109(C7):1–10. doi:10.1029/2003JC002242

Timmermann R, Goosse H, Madec G, Fichefet T, Ethe C, Valérie D (2005) On the representation of high latitude processes in the ORCA-LIM global coupled sea ice-cean model. Ocean Modell 8(1–2):175–201. doi:10.1016/j.ocemod.2003.12.009

Tonboe RT, Eastwood S, Lavergne T, Sørensen AM, Rathmann N, Dybkjær G, Pedersen LT, Høyer JL, Kern S (2016) The EUMETSAT sea ice concentration climate data record. Cryosphere 10(5):2275–2290. doi:10.5194/tc-10-2275-2016

Trenberth KE, Large WG, Olson JG (1989) Global Ocean Wind Stress, climatology and monthly, by Trenberth et al. Digital media. National Center for Atmospheric Research, Boulder

Tsamados M, Feltham DL, Wilchinsky AV (2013) Impact of a new anisotropic rheology on simulations of Arctic sea ice. J Geophys Res Oceans 118(1):91–107. doi:10.1029/2012JC007990

Tsamados M, Feltham DL, Schroeder D, Flocco D, Farrell SL, Kurtz N, Laxon SW, Bacon S (2014) Impact of variable atmospheric and oceanic form drag on simulations of Arctic sea ice. J Phys Oceanogr 44(5):1329–1353. doi:10.1175/JPO-D-13-0215.1

Turner J, Bracegirdle TJ, Phillips T, Marshall GJ, Hosking JS (2013) An initial assessment of antarctic sea ice extent in the CMIP5 models. J Clim 26(5):1473–1484. doi:10.1175/JCLI-D-12-00068.1

Turner J, Hosking JS, Marshall GJ, Phillips T, Bracegirdle TJ (2016) Antarctic sea ice increase consistent with intrinsic variability of the Amundsen Sea Low. Clim Dyn 46(7):2391–2402. doi:10.1007/s00382-015-2708-9

Uotila P, O'Farrell S, Marsland S, Bi D (2012) A sea-ice sensitivity study with a global ocean-ice model. Ocean Modell 51:1–18. doi:10.1016/j.ocemod.2012.04.002

Uotila P, Holland P, Vihma T, Marsland S, Kimura N (2014) Is realistic Antarctic sea-ice extent in climate models the result of excessive ice drift? Ocean Modell 79:33–42. doi:10.1016/j.ocemod.2014.04.004

Uotila P, Iovino D, Vancoppenolle M, Lensu M, Rousset C (2017) Comparing sea ice, hydrography and circulation between NEMO3.6 LIM3 and LIM2. Geosci Model Dev 10(2):1009–1031. doi:10.5194/gmd-10-1009-2017

Vancoppenolle M, Fichefet T, Goosse H, Bouillon S, Madec G, Morales Maqueda MA (2009) Simulating the mass balance and salinity of Arctic and Antarctic sea ice. 1. Model description and validation. Ocean Modell 27(1–2):33–53. doi:10.1016/j.ocemod.2008.10.005

Vancoppenolle M, Timmermann R, Ackley SF, Fichefet T, Goosse H, Heil P, Leonard KC, Lieser J, Nicolaus M, Papakyriakou T, Tison JL (2011) Assessment of radiation forcing data sets for large-scale sea ice models in the Southern Ocean. Deep-Sea Res Pt II 58(9–10):1237–1249. doi:10.1016/j.dsr2.2010.10.039

Vihma T, Uotila J, Cheng B, Launiainen J (2002) Surface heat budget over the Weddell Sea: Buoy results and model comparisons. J Geophys Res 107(C2):5–1–5–15. doi:10.1029/2000JC000372

Wang Y, Zhou D, Bunde A, Havlin S (2016) Testing reanalysis data sets in Antarctica: Trends, persistence properties, and trend significance. J Geophys Res Atmos 121(21):12,839–12,855. doi:10.1002/2016JD024864

Wilchinsky AV, Heorton HDBS, Feltham DL, Holland PR (2015) Study of the impact of ice formation in leads upon the sea ice pack mass balance using a new frazil and grease ice parameterization. J Phys Oceanogr 45(8):2025–2047. doi:10.1175/JPO-D-14-0184.1

Worby AP, Geiger CA, Paget MJ, Van Woert ML, Ackley SF, DeLiberty TL (2008) Thickness distribution of Antarctic sea ice. J Geophys Res 113(C5):C05S92. doi:10.1029/2007JC004254

Zunz V, Goosse H, Massonnet F (2013) How does internal variability influence the ability of CMIP5 models to reproduce the recent trend in Southern Ocean sea ice extent? Cryosphere 7(2):451–468. doi:10.5194/tc-7-451-2013

Zweng M, Reagan J, Antonov J, Locarnini R, Mishonov A, Boyer T, Garcia H, Baranova O, Johnson D, DSeidov, Biddle M (2013) World Ocean Atlas 2013, Volume 2: Salinity. In: Levitus S (ed) mishonov technical ed., noaa atlas nesdis a. National Centers for Environmental Information, p 74, 39